Supplementary materials for paper “Evaluating the radiative fidelity of PALM (v25.04) in high-resolution: impact of diverse urban morphology and vegetation on short-wave radiation“

Jelena Radović[1], Michal Belda[1], Martin Bureš[2], Kryštof Eben[2], Jan Geletič[1,2], Jakub Jura[3], Pavel Krč[2], Hynek Řezníček[2], and Jaroslav Resler[2]

[1]Department of Atmospheric Physics, Faculty of Mathematics and Physics, Charles University Prague, V Holešovičkách 2, 180 00 Prague 8, Czech Republic

[2]Department of Complex Systems, Institute of Computer Science of the Czech Academy of Sciences, Pod Vodárenskou věží 271/2, 182 00 Prague, Czech Republic

[3]Department of Instrumentation and Control Engineering, Faculty of Mechanical Engineering, Czech Technical University in Prague, Technická 4, 166 07 Praha 6, Czech Republic

Correspondence: Jelena Radović (jelena.radovic@matfyz.cuni.cz)

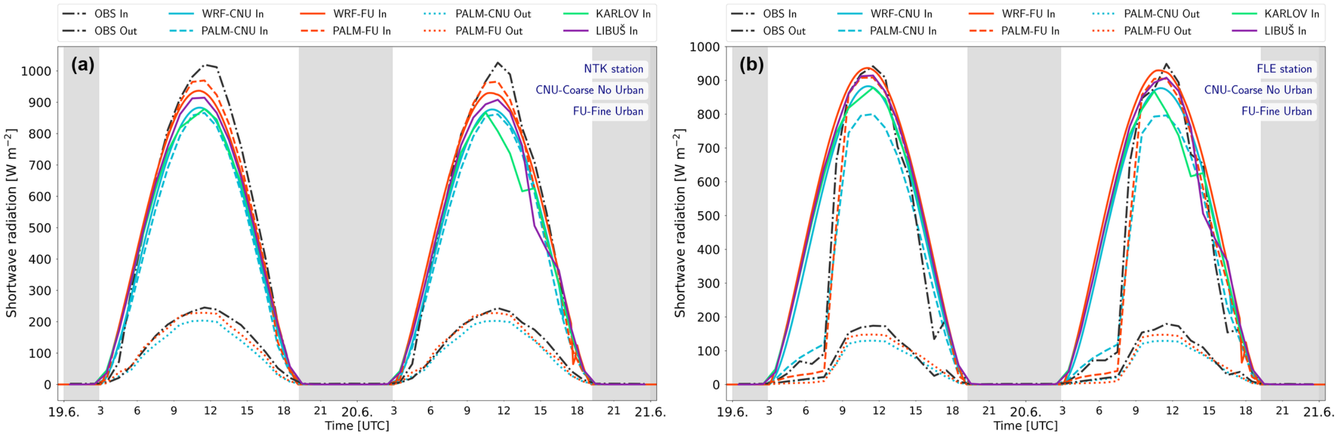

Figure S1. The comparison of observed hourly averages of incoming (In) and outgoing (Out) short-wave radiation for the e1 episode at the stations NTK (a) and FLE (b), with PALM model outputs for both WRF configurations. Additional lines represent the raw WRF outputs, Coarse No Urban (WRF-CNU), and Fine Urban (WRF-FU), and measurements from professional meteorological stations in Karlov and Libuš.

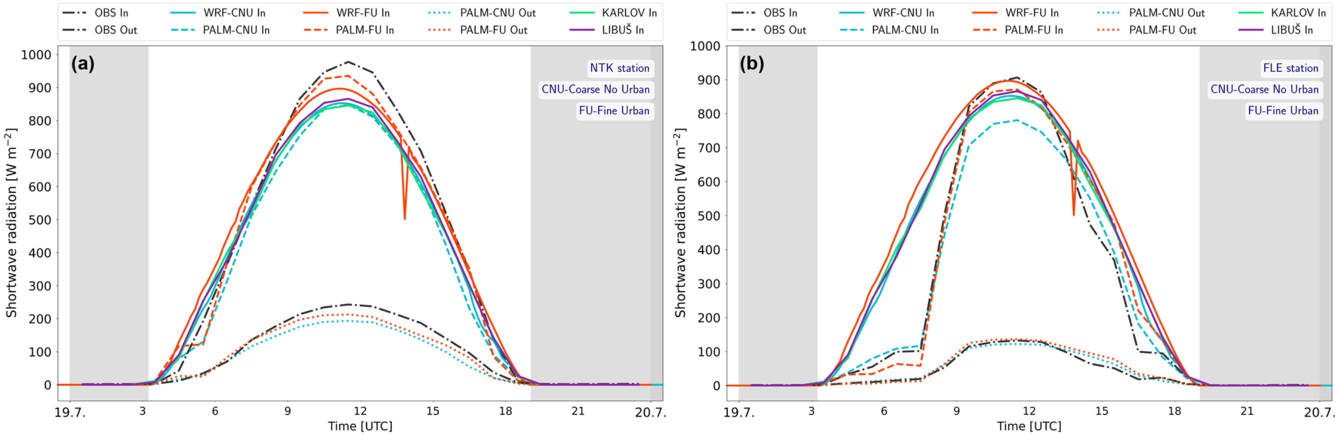

Figure S2. The comparison of observed hourly averages of incoming (In) and outgoing (Out) short-wave radiation for the e2 episode at the stations NTK (a) and FLE (b), with PALM model outputs for both WRF configurations. Additional lines represent the raw WRF outputs, Coarse No Urban (WRF-CNU), and Fine Urban (WRF-FU), and measurements from professional meteorological stations in Karlov and Libuš.

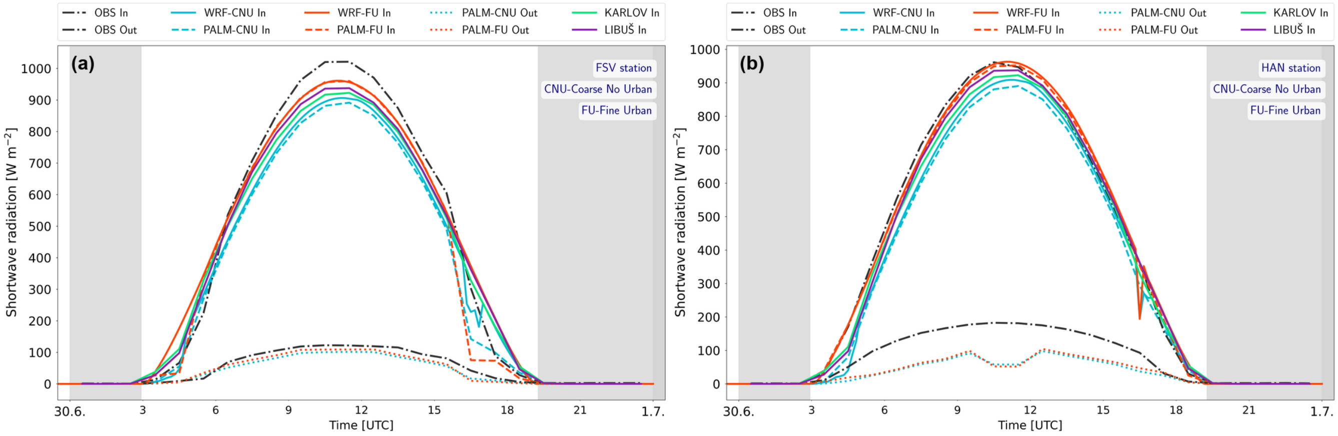

Figure S3. The comparison of observed hourly averages of incoming (In) and outgoing (Out) short-wave radiation for the e4 episode at the stations FSV (a) and HAN (b), with PALM model outputs for both WRF configurations. Additional lines represent the raw WRF outputs, Coarse No Urban (WRF-CNU), and Fine Urban (WRF-FU), and measurements from professional meteorological stations in Karlov and Libuš.

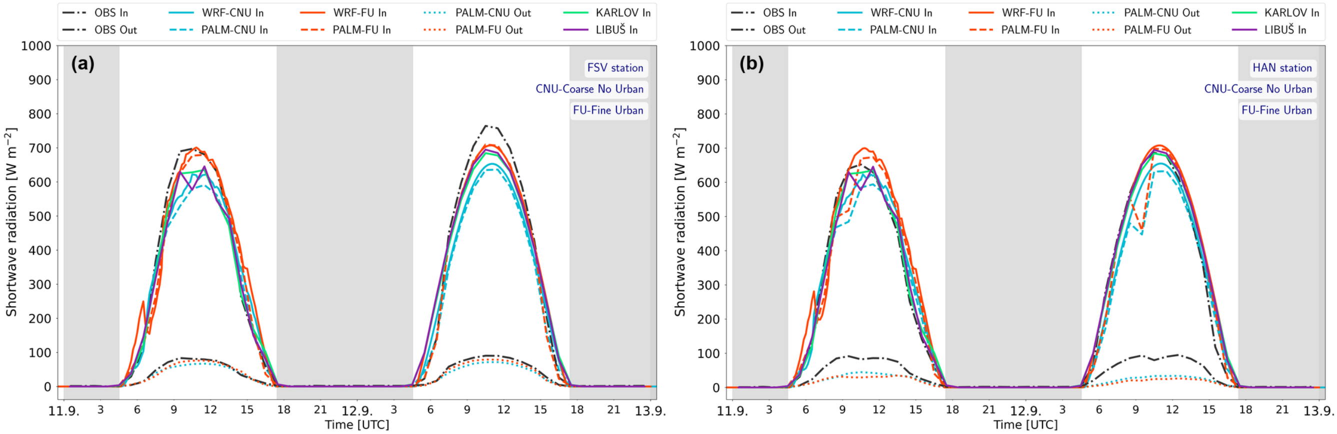

Figure S4. The comparison of observed hourly averages of incoming (In) and outgoing (Out) short-wave radiation for the e6 episode at the stations FSV (a) and HAN (b), with PALM model outputs for both WRF configurations. Additional lines represent the raw WRF outputs, Coarse No Urban (WRF-CNU), and Fine Urban (WRF-FU), and measurements from professional meteorological stations in Karlov and Libuš.

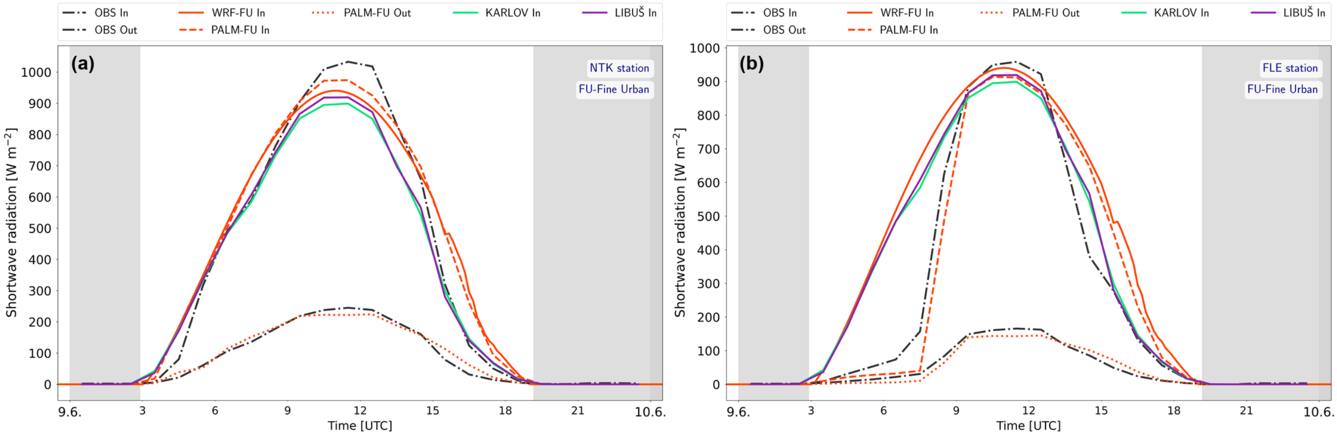

Figure S5. The comparison of observed hourly averages of incoming (In) and outgoing (Out) short-wave radiation for the e7 episode at the stations NTK (a) and FLE (b), with PALM model output for WRF Fine Urban (WRF-FU) configuration. Additional lines represent the raw WRF output, Fine Urban (WRF-FU), and measurements from professional meteorological stations in Karlov and Libuš.

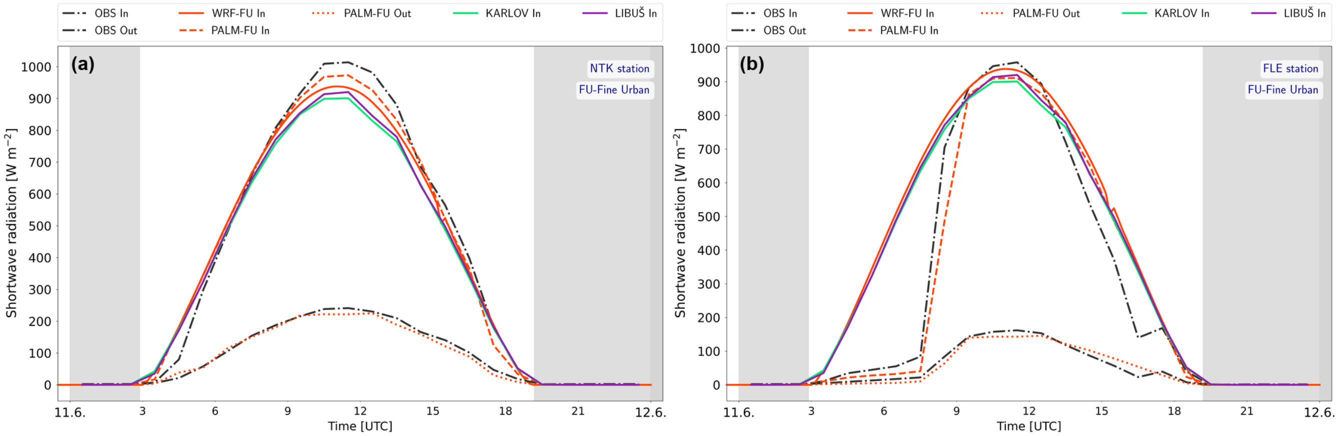

Figure S6. The comparison of observed hourly averages of incoming (In) and outgoing (Out) short-wave radiation for the e8 episode at the stations NTK (a) and FLE (b), with PALM model output for WRF Fine Urban (WRF-FU) configuration. Additional lines represent the raw WRF output, Fine Urban (WRF-FU), and measurements from professional meteorological stations in Karlov and Libuš.

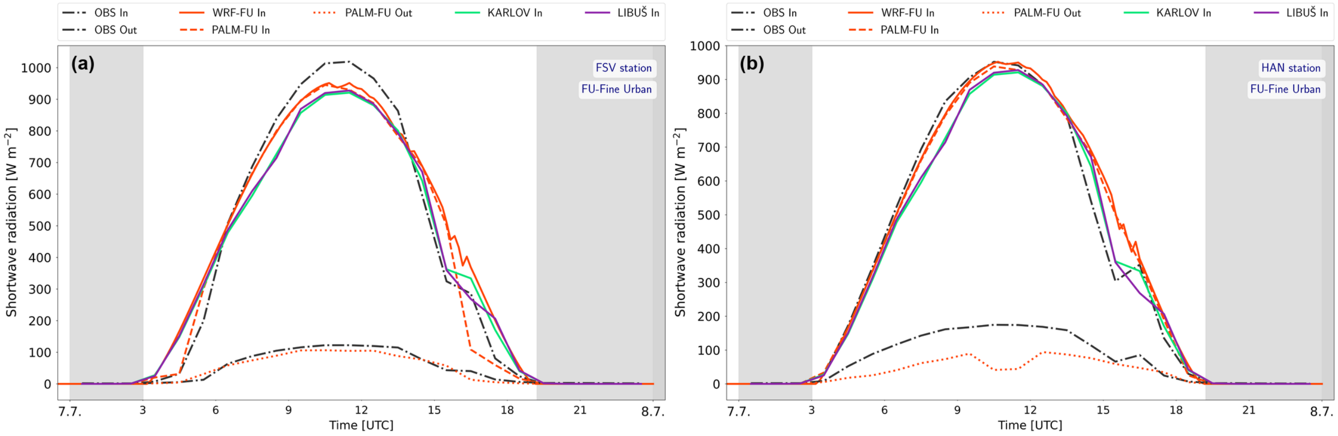

Figure S7. The comparison of observed hourly averages of incoming (In) and outgoing (Out) short-wave radiation for the e11 episode at the stations FSV (a) and HAN (b), with PALM model output for WRF Fine Urban (WRF-FU) configuration. Additional lines represent the raw WRF output, Fine Urban (WRF-FU), and measurements from professional meteorological stations in Karlov and Libuš.

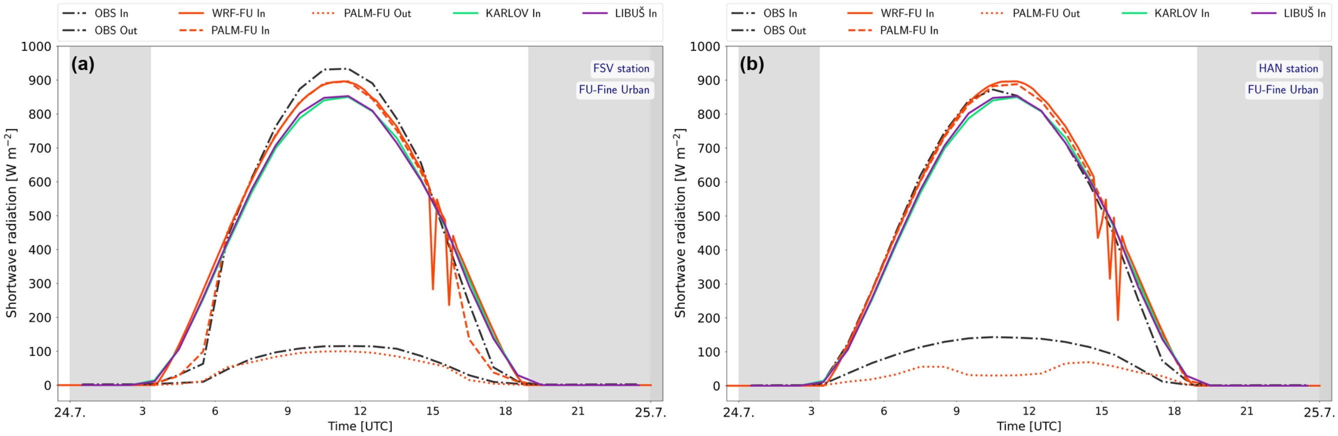

Figure S8. The comparison of observed hourly averages of incoming (In) and outgoing (Out) short-wave radiation for the e13 episode at the stations FSV (a) and HAN (b), with PALM model output for WRF Fine Urban (WRF-FU) configuration. Additional lines represent the raw WRF output, Fine Urban (WRF-FU), and measurements from professional meteorological stations in Karlov and Libuš.

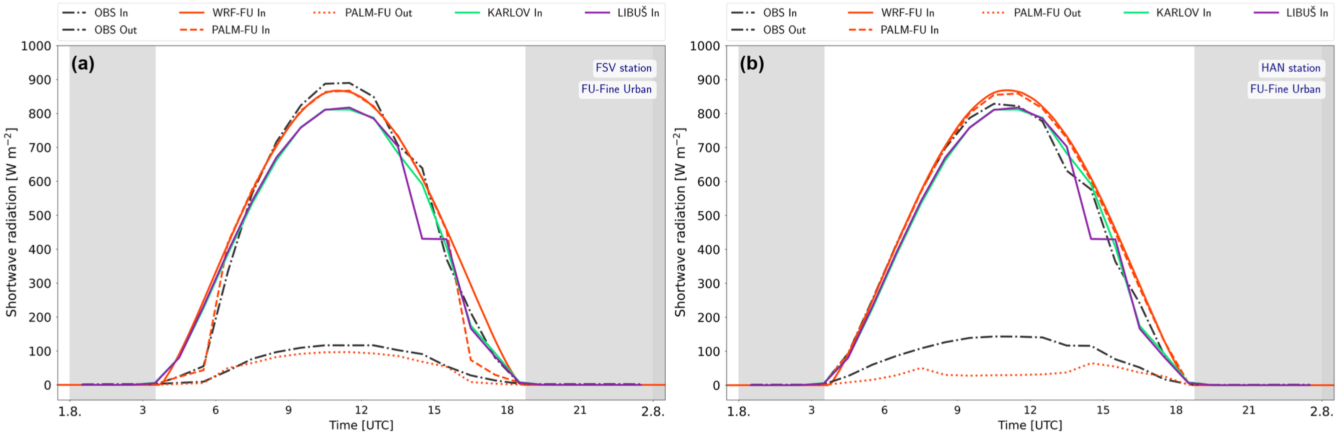

Figure S9. The comparison of observed hourly averages of incoming (In) and outgoing (Out) short-wave radiation for the e14 episode at the stations FSV (a) and HAN (b), with PALM model output for WRF Fine Urban (WRF-FU) configuration. Additional lines represent the raw WRF output, Fine Urban (WRF-FU), and measurements from professional meteorological stations in Karlov and Libuš.

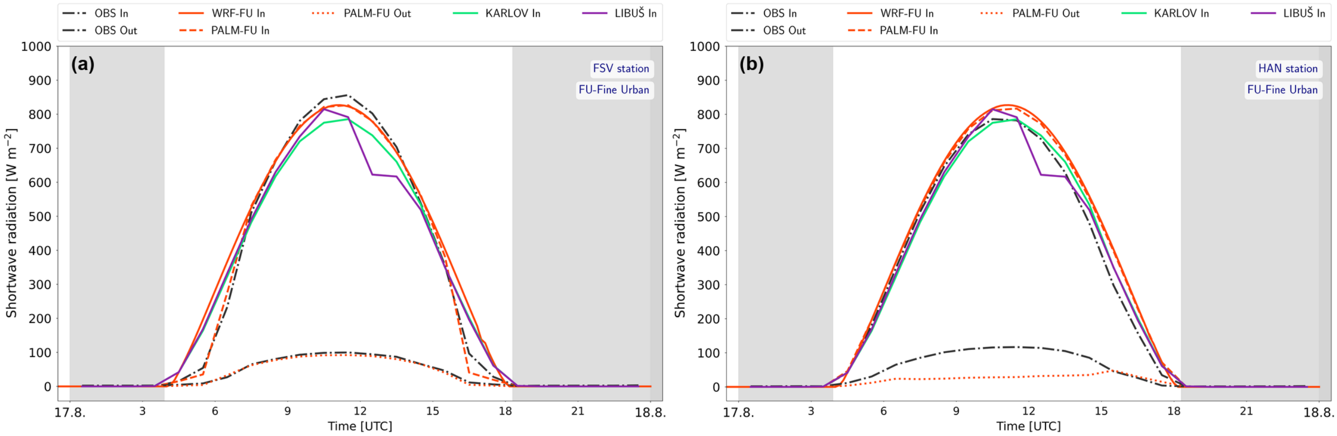

Figure S10. The comparison of observed hourly averages of incoming (In) and outgoing (Out) short-wave radiation for the e15 episode at the stations FSV (a) and HAN (b), with PALM model output for WRF Fine Urban (WRF-FU) configuration. Additional lines represent the raw WRF output, Fine Urban (WRF-FU), and measurements from professional meteorological stations in Karlov and Libuš.

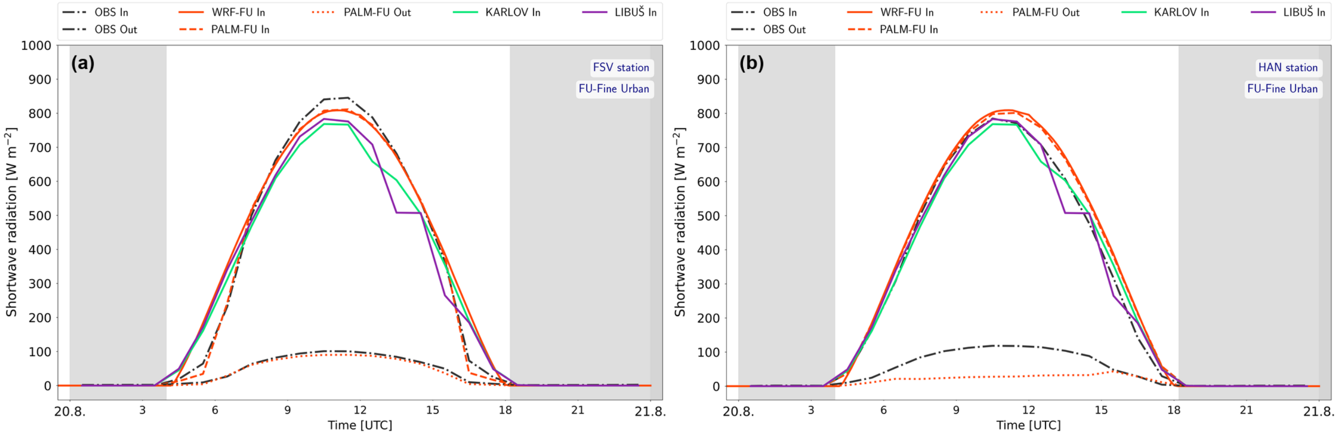

Figure S11. The comparison of observed hourly averages of incoming (In) and outgoing (Out) short-wave radiation for the e16 episode at the stations FSV (a) and HAN (b), with PALM model output for WRF Fine Urban (WRF-FU) configuration. Additional lines represent the raw WRF output, Fine Urban (WRF-FU), and measurements from professional meteorological stations in Karlov and Libuš.

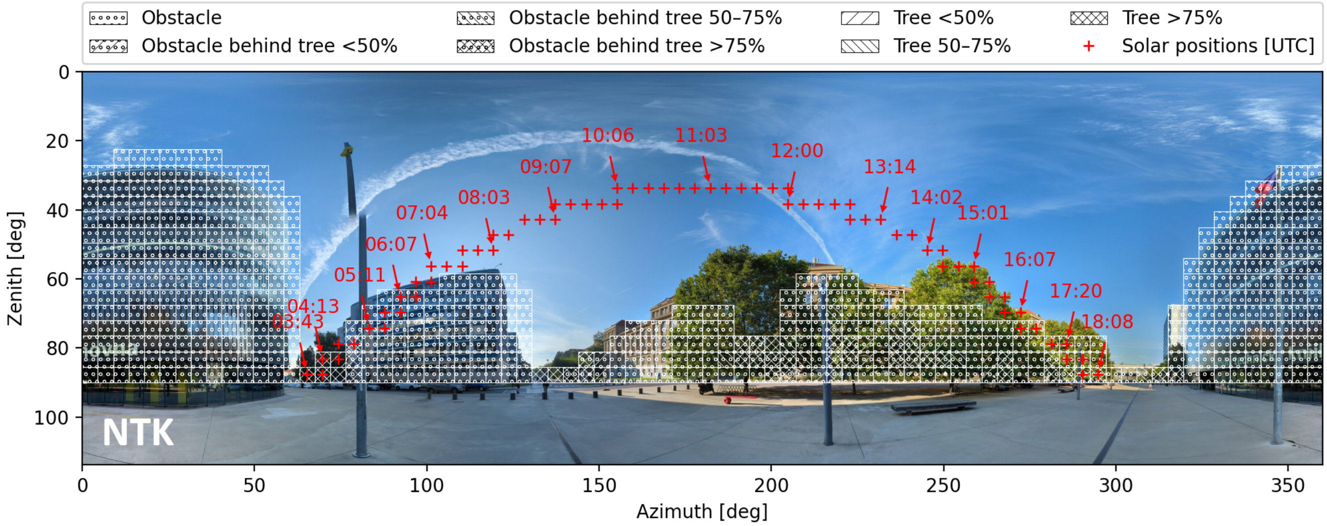

Figure S12. Hemispherical view at the NTK observation site with obstructions and vegetation as modelled by PALM, plotted in azimuth–zenith coordinates. Trees and obstacles are classified according to their fractional area coverage. Red crosses indicate the Sun's trajectory throughout the day, with annotated timestamps in UTC.

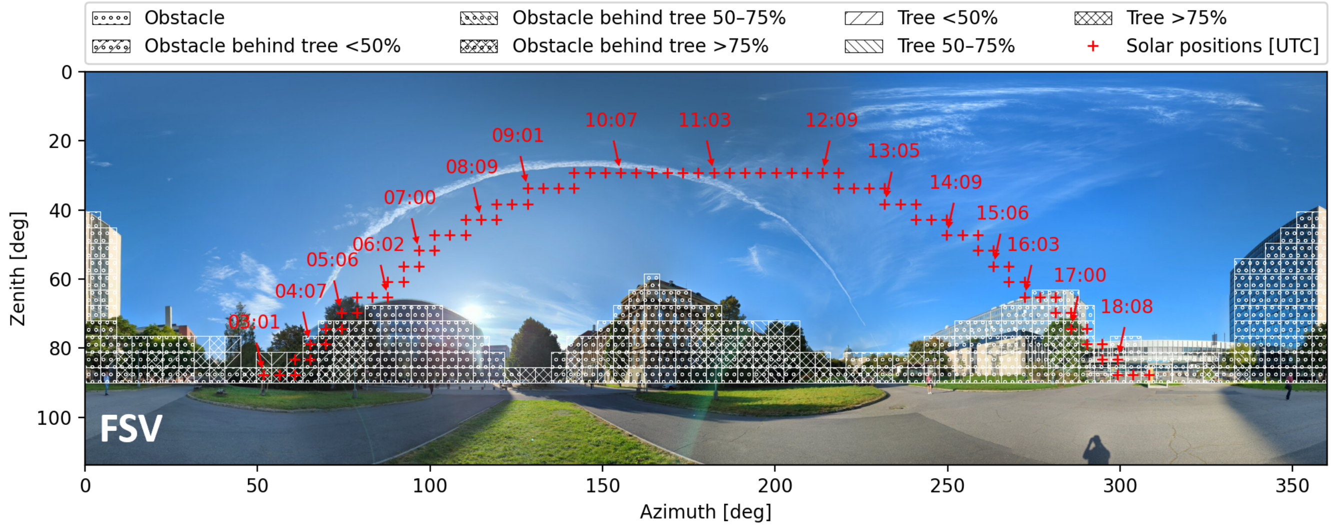

Figure S13. Hemispherical view at the FSV observation site with obstructions and vegetation as modelled by PALM, plotted in azimuth–zenith coordinates. Trees and obstacles are classified according to their fractional area coverage. Red crosses indicate the Sun's trajectory throughout the day, with annotated timestamps in UTC.

Table S1. Synoptic weather types and frontal systems crossing through Prague during selected episodes in 2017 and 2018.

Date	Weather type	Front crossings			
		Crossing time [UTC]	Type	Direction (from)	Intensity
2017					
09 June	Western anticyclone of summer type (Wal)	18 23	Cold Cold	West West	Medium Medium
11 June	Western anticyclone of summer type (Wal)	7 22	Warm Warm	South West South West	Weak Weak
19–20 June	Anticyclone/ Travelling anticyclone (A/Ap)	9 (20 Jun.)	Cold	North West	Weak
07 July	Western cyclone (Wc)	1	Cold	Western	Medium
19 July	Western anticyclone of summer type (Wal)	No data	No data	No data	No data
07 August	Traveling anticyclone (Ap)	No data	No data	No data	No data
2018					
16 June	North East anticyclone (Nea)	No data	No data	No data	No data
30 June	North East anticyclone (Nea)	No data	No data	No data	No data
02–03 July	North West anticyclone (NWa)	No data	No data	No data	No data
07 July	North West anticyclone (NWa)	17	Occlusive	North West	Weak
21 July	Low pressure trough (B)	17	Occlusive	South West	Medium
24 July	North West anticyclone (NWa)	No data	No data	No data	No data
01 August	Eastern anticyclone (Ea)	No data	No data	No data	No data
17 August	Western anticyclone of summer type (Wal)	23	Cold	West	Medium
20 August	Western anticyclone of summer type (Wal)	2 15	Warm Cold	West North West	Weak Medium
11–12 September	Western anticyclone of summer type (Wal)	2 (11 Sept.) 9 (11 Sept.) 12 Sept.	Occlusive Warm No data	West West No data	Medium Medium No data

Table S2. WRF albedo during 2017 and 2018 at observation stations. WRF–1 km domain.

Date	Station	Mean Albedo	Albedo at Noon	Albedo (Noon Avg. +-1 h)
		2017		
09 June	FLE	0.199	0.156	0.156
	NTK	0.199	0.156	0.156
11 June	FLE	0.173	0.156	0.157
	NTK	0.173	0.156	0.157
19–20 June	FLE	0.174	0.167	0.157
	NTK	0.174	0.167	0.157
07 July	FLE	0.213	0.353	0.228
	NTK	0.213	0.353	0.228
19 July	FLE	0.181	0.157	0.156
	NTK	0.181	0.157	0.156
07 August	FLE	0.180	0.155	0.155
	NTK	0.180	0.155	0.155
		2018		
16 June	FSV	0.197	0.156	0.157
	HAN	0.213	0.158	0.158
30 June	FSV	0.172	0.156	0.156
	HAN	0.172	0.158	0.158
02–03 July	FSV	0.173	0.167	0.157
	HAN	0.173	0.167	0.158
07 July	FSV	0.184	0.176	0.192
	HAN	0.183	0.179	0.191
21 July	FSV	0.206	0.169	0.169
	HAN	0.206	0.169	0.169
24 July	FSV	0.184	0.156	0.156
	HAN	0.184	0.158	0.158
01 August	FSV	0.176	0.164	0.163
	HAN	0.176	0.163	0.163
17 August	FSV	0.171	0.154	0.154
	HAN	0.172	0.156	0.156
20 August	FSV	0.170	0.154	0.154
	HAN	0.171	0.156	0.156
11–12 September	FSV	0.190	0.313	0.168
	HAN	0.192	0.309	0.171

Table S3. WRF albedo during 2017 and 2018 at observation stations. WRF–3 km domain.

Date	Station	Mean Albedo	Albedo at Noon	Albedo (Noon Avg. +-1 h)
		2017		
19–20 June	FLE	0.144	0.144	0.144
	NTK	0.144	0.144	0.144
19 July	FLE	0.140	0.140	0.140
	NTK	0.140	0.140	0.140
07 August	FLE	0.135	0.135	0.135
	NTK	0.135	0.135	0.135
		2018		
30 June	FSV	0.142	0.142	0.142
	HAN	0.152	0.152	0.152
02–03 July	FSV	0.142	0.142	0.142
	HAN	0.151	0.151	0.151
11–12 September	FSV	0.126	0.127	0.126
	HAN	0.132	0.133	0.132

Table S4. Average albedo values per station. WRF–1 km domain.

Station	Avg (Mean)	Avg (Noon)	Avg (Noon Avg)
FLE [213, 149]	0.187	0.190	0.168
NTK [213, 149]	0.187	0.190	0.168
FSV [213, 149]	0.182	0.176	0.162
HAN [213, 148]	0.184	0.177	0.163

Table S5. Average albedo values per station. WRF–3 km domain.

Station	Avg (Mean)	Avg (Noon)	Avg (Noon Avg)
FLE [75, 70]	0.139	0.140	0.139
NTK [75, 70]	0.139	0.140	0.139
FSV [75, 70]	0.137	0.137	0.137
HAN [75, 69]	0.145	0.145	0.145

1 Statistical evaluation

Considering that M_i is the PALM-simulated value, $\overline{M}$ is the mean of all PALM-simulated values, O_i is the observed value, $\overline{O}$ is the mean of the observations, and n is the total number of paired samples, the following formulas are applied for the statistical evaluation:

1.1 Mean Bias Error MBE

$$\mathrm{MBE} = \tfrac{1}{n}\textstyle\sum_{i=1}^{n}(M_i - O_i)$$

1.2 Root Mean Square Error RMSE

$$\mathrm{RMSE} = \sqrt{\tfrac{1}{n}\textstyle\sum_{i=1}^{n}(M_i - O_i)^2}$$

1.3 Pearson correlation coefficient r

$$\mathrm{r} = \frac{\sum_{i=1}^{n}(M_i - \overline{M})(O_i - \overline{O})}{\sqrt{\sum_{i=1}^{n}(M_i - \overline{M})^2 - \sum_{i=1}^{n}(O_i - \overline{O})^2}}$$

1.4 Coefficient of determination R^2

$$\mathrm{R}^2 = 1 - \frac{\sum_{i=1}^{n}(O_i - M_i)^2}{\sum_{i=1}^{n}(O_i - \overline{O})^2}$$

1.5 Spearman's correlation coefficient ρ

$$\rho = 1 - \frac{6\sum_{i=1}^{n} d_i^2}{n(n^2-1)}; d_i = \mathrm{rank}(M_i) - \mathrm{rank}(O_i)$$

1.6 Kendall's correlation coefficient τ

$$\tau = \frac{N_c - N_d}{\frac{1}{2}n(n^2-1)}; \text{where } N_c \text{ and } N_d \text{ are the numbers of concordant and discordant pairs, respectively.}$$

1.7 Index of Agreement (d; Willmott, 1981)

$$d = 1 - \frac{\sum_{i=1}^{n}(M_i - O_i)^2}{\sum_{i=1}^{n}(|M_i - \overline{O}| + |O_i - \overline{O}|)^2}$$

1.8 Absolute difference AD

$$\mathrm{AD} = \frac{1}{n}\sum_{i=1}^{n}|M_i - O_i|$$

1.9 Relative Difference RD

$$\mathrm{RD} = \frac{1}{n}\sum_{i=1}^{n}\left(\frac{M_i - O_i}{O_i}\right) \times 100\%$$

References

Willmott, C. J.: ON THE VALIDATION OF MODELS, Physical Geography, 2, 184–194, https://doi.org/10.1080/02723646.1981.10642213, 1981.